Strain-Induced Quasi-1D Channels in Twisted Moiré Lattices

Andreas Sinner [1,2,*] Pierre A. Pantaleón [1,†] and Francisco Guinea [1,3,4]

[1]*IMDEA Nanoscience, Faraday 9, 28049 Madrid, Spain*
[2]*Institute of Physics, University of Opole, 45-052 Opole, Poland*
[3]*Donostia International Physics Center, Paseo Manuel de Lardizábal 4, 20018 San Sebastián, Spain*
[4]*Ikerbasque, Basque Foundation for Science, 48009 Bilbao, Spain*

We study the effects of strain in moiré systems composed of honeycomb lattices. We elucidate the formation of almost perfect one-dimensional moiré patterns in twisted bilayer systems. The formation of such patterns is a consequence of an interplay between twist and strain which gives rise to a collapse of the reciprocal space unit cell. As a criterion for such collapse we find a simple relation between the two quantities and the material specific Poisson ratio. The induced one-dimensional behavior is characterized by two, usually incommensurate, periodicities. Our results offer explanations for the complex patterns of one-dimensional channels observed in low angle twisted bilayer graphene systems and twisted bilayer dicalcogenides. Our findings can be applied to any hexagonal twisted moiré pattern and can be easily extended to other geometries.

Introduction.—Twisted bilayer and multilayer systems represent two-dimensional materials, where atom-thick layers of the same or different materials are superimposed and rotated by an arbitrary twist angle. Twisted bilayer graphene (TBG) represents arguably the most prominent physical system of this kind [1–6], the bilayers of transition metal dicalcogenides (TMD) the other [7–15]. The effect of twisting two periodic systems with respect to each other results in the formation of superlattices, the moiré patterns [16,17]. In TBG such moiré patterns give rise to very narrow bands at small twist angles, which can host correlated electronic states and superconductivity [18–20]. In addition, strains are ubiquitous in moiré systems [21]. The interplay of electronic and elastic degrees of freedom in moiré systems is not fully understood [22–24]. The effect of strains in monolayer graphene and other nontwisted bidimensional materials has been extensively studied [25–29]. Important insights on the role of strains in twisted bilayer graphene were reported in [30,31]. The applied in-plane strain acting on both sublattices in opposite directions changes the distance between the nearest lattice atoms within each layer, and increases correspondingly the electronic hopping amplitude between them. In terms of the effective Dirac description of graphene, this effect creates an additional term which resembles the conventional vector potential, which however does not break the time-reversal symmetry of the Hamiltonian [25,32–37]. This term displaces the Dirac points from their original positions but does not distort the shape of the Brillouin zone. This process breaks the $\mathbf{C_6}$ symmetry of the Dirac points and lifts the degeneracy of the saddle points. At larger strains the system goes through a Lifshitz transition characterized by a fusion of the Dirac

points with resulting anisotropic spectrum and different scaling behavior of the low-energy part of the density of states [32–37].

Similar effects might be expected for strained twisted bilayer graphene, such as the appearance of higher Van Hove singularities [31,38,39]. However the plethora of observed phenomena in strained twisted bilayer graphene is much larger than suggested by those analogies. For instance, the observation of highly anisotropic moiré patterns in the strained twisted bilayer graphene has been reported in many experiments [40–52]. With increasing strain the degree of deformation of the unit cells increases as well, until they become effectively one-dimensional stripes.

In this Letter, we show how the deformation of the moiré superlattice, and the emergence of quasi-1D features are a consequence of the interplay between twist and strain. As a criterion for such transition we find a simple relation between the applied uniaxial strain, the twist angle, and the material dependent Poisson ratio.

Initially, the moiré Brillouin zone (mBZ) has the form of a perfect honeycomb cell. With increasing strain it gets deformed and elongated in a selected direction, until it reduces to a line at the critical strain value. The selected direction is determined by the material dependent parameters. We construct the strain dependent lattice vectors in both real and reciprocal spaces and explore the consequences of this transition for the spectra and the density of states of twisted bilayer graphene within a continuum model approximation [1,4,53,54]. In the one-dimensional limit we obtain electronic bands, which are determined by an interplay of two generally different and incommensurate

periodicities. These can be fine-tuned to a single periodicity by varying external applied forces.

Geometry of the deformed mBZ.—We consider the case of a twisted bilayer honeycomb lattice, following the approach in [31]. We chose the reciprocal lattice vectors for each monolayer system as $\mathbf{b}_{1,2} = 2\pi a^{-1}(1, \mp 1/\sqrt{3})$, with lattice constant a (for graphene $a \approx 2.46$ Å). The reciprocal lattice vectors of the twisted layers are obtained by rotating vectors $\mathbf{b}_i$ by a twist angle, i.e. $\mathbf{G}_i^{\uparrow,\downarrow} = R[\mp\theta/2]\mathbf{b}_i$. Here, $\uparrow(\downarrow)$ and $-(+)$ refer to the upper (lower) layer, with $R[\pm\theta]$ being the usual rotation matrix, cf. Eq. (S4) in the Supplemental Material [55].

The reciprocal lattice vectors of the moiré superlattice are $\mathbf{g}_i = \mathbf{G}_i^{\uparrow} - \mathbf{G}_i^{\downarrow}$. Being subject to the geometric deformation by strain they change to

$$\tilde{\mathbf{g}}_i = \tilde{\mathbf{G}}_i^{\uparrow} - \tilde{\mathbf{G}}_i^{\downarrow} = \mathbf{T}\mathbf{b}_i, \tag{1}$$

where the transformation matrix $\mathbf{T}$ is

$$\mathbf{T} = (\mathbb{1} - \mathcal{E}^{\uparrow})R[-\theta/2] - (\mathbb{1} - \mathcal{E}^{\downarrow})R[+\theta/2], \tag{2}$$

with the symmetric strain tensor $\mathcal{E}^\ell = \{\epsilon_{i,j}^\ell\}$, $i,j = \{x,y\}$, and $\ell = \uparrow,\downarrow$. In the experimentally relevant case of uniaxial heterostrain, in which forces are applied along one direction one makes a simplification $\mathcal{E}^\downarrow = -\mathcal{E}^\uparrow = \mathcal{E}/2$ [30]. In particular, the uniaxial heterostrain can be parametrized in terms of two quantities: the dimensionless strain magnitude ϵ measured with respect to the lattice spacing, and the strain direction determined by the angle ϕ. The strain tensor is then a function of ϵ, ϕ, and the Poisson ratio ν of the system's monolayers [55]. For monolayer graphene this value is roughly $\nu \approx 0.16$. Here we emphasize that our considerations include but are not restricted to the only case of the honeycomb uniaxial heterostrain. Note that when forces along two perpendicular directions are applied, the strains $\epsilon_{\parallel,\parallel}$ and $\epsilon_{\perp,\perp}$ can be tuned separately.

Collapse of the mBZ for a critical value of the strain.—In Fig. 1 we show the real and reciprocal space of a twisted moiré lattice. As the strain increases, the unit cell in real space is enlarged and rotated with a tendency toward a particular spatial direction. In reciprocal space, the mBZ zone gets progressively squeezed until it collapses at a certain critical value. This collapse implies that the vectors $\tilde{\mathbf{g}}_i$ in Eq. (1) are collinear, which occurs when $\mathbf{T}\mathbf{b}_i = \alpha_i\mathbf{s}$, $i = 1, 2$ for vector $\mathbf{s}$ to be determined and real α_i. Combining the equations we get

$$\mathbf{T}\left[\mathbf{b}_1 - \frac{\alpha_1}{\alpha_2}\mathbf{b}_2\right] = \mathbf{0}. \tag{3}$$

Since $\mathbf{b}_i$ are linearly independent, number α that $\alpha\mathbf{b}_i = \mathbf{b}_j$ for $i \neq j$, the above equation is satisfied only if
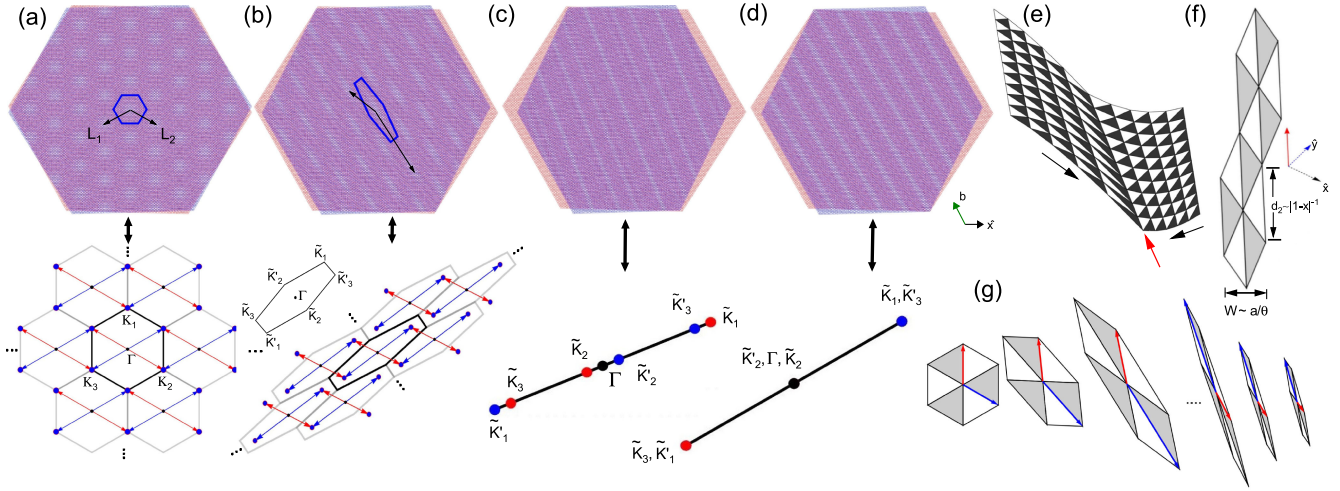
$$\det\{\mathbf{T}\} = 0. \tag{4}$$

FIG. 1. Strain-induced geometrical effects in a moiré superlattice with twist angle $\theta = 3°$. The real space geometry of a twisted honeycomb bilayer subject to uniaxial heterostrain with Poisson ratio $\nu = 0.165$ and strength (a) $\epsilon = 0\epsilon_c$, (b) $\epsilon = 0.5\epsilon_c$, and (c) $\epsilon = 1.0\epsilon_c$. In (d) $\epsilon = 1.0\epsilon_c$ and $\nu = 1/3$, ϵ_c referred to as the critical strain value from Eq. (5). In (a)(b) the blue hexagon visualizes the lattice unit cell. At the bottom of each moiré structure the corresponding reciprocal space is shown. Here, the colored arrows point to the geometrical positions of the Dirac points. In (d) we show the formation of quasi-1D channels due to a commensurate condition between the lattice vectors (see the main text). (e) The formation of an edge domain wall, emphasized by the red arrow, due to a nonuniform strain. Bright (dark) triangles emphasize the AB (BA) stacking domains. Black arrows indicate the direction of the strain increasing from zero to a finite value, chosen here as $0.5\epsilon_c$. (f) Critical strain scales in real space for two unit cells. For visualization purposes, the hexagons have been rotated, as indicated by the $\hat{x}\hat{y}$ axes. (g) Stacking domain cells calculated for $\epsilon = \{0, 0.25, 0.50, 1.3, 1.4, 1.5\}\epsilon_c$, from left to right.

Equation (4) represents one of our main results. It is very general and does not assume any specific lattice of the monolayer (i.e., honeycomb, square, etc.), nor any specific type of the strain. For the particular case of the uniaxial heterostrain, the collapse condition, Eq. (4), reduces to

$$\epsilon_c = \pm \frac{2}{\sqrt{\nu}} \tan\frac{\theta}{2}, \qquad (5)$$

which is independent of the angle ϕ, and ϵ_c denotes the critical strain strength. The linearization of Eq. (5) $\epsilon_c \approx \pm\theta/\sqrt{\nu}$ is reasonable for $\theta < 10°$. This result implies that for a small angle moiré lattice the critical strain should be within the experimental range. For example, for TBG with a marginal twist angle $\theta < 0.2°$, a uniaxial heterostrain lower than 1.0% is required to collapse the mBZ, and this creates uni-dimensional channels. Equation (4) can always be satisfied when the ratio between the interatomic distance and the moiré unit length tends to zero. The case of comparable competing length scales, in which additional patterns like those observed in graphene on black phosphorous [26] may occur, is not considered here. Our results show an impressive accuracy when compared with the experimental data obtained from the observations of the uni-dimensional domain formation in multilayer graphene systems [40,42,50,52], transition metal dicalcohenides [43,66], and graphene on multilayer black phosphorus [26]. For instance, Refs. [42] and [66] contain quantitative estimations for the formation of the sloped quasi-1D stripes: Ref. [42] reports $\epsilon = 15\%$ for $\theta = 4°$, whilst our Eq. (5) yields $\epsilon_c \approx 17.5\%$. Reference [66] quotes $\epsilon = 8\%$ for $\theta = 2°$, whilst our model's prediction is at $\epsilon_c \approx 8\%$ (with $\nu \approx 0.19$ for TMD [67]).

Geometry of the deformed honeycomb moiré lattice.— We now explore the consequences of the collapsing conditions obtained in the previous section. For simplicity but without loss of generality we assume that the strain direction is along the x axis, i.e., for $\phi = 0$. The six corners of the zigzag oriented monolayer honeycomb Brillouin zone

$$\mathbf{K}_1 = k_0 \begin{pmatrix} -2 \\ 0 \end{pmatrix}, \mathbf{K}_{2,3} = k_0 \begin{pmatrix} 1 \\ \pm\sqrt{3} \end{pmatrix}, \qquad (6)$$

and $\mathbf{K}_1' = -\mathbf{K}_3$, $\mathbf{K}_2' = -\mathbf{K}_1$, and $\mathbf{K}_3' = -\mathbf{K}_2$, where $k_0 = 2\pi(3a)^{-1}$. Thus, the six corners of the deformed armchair oriented mBZ are obtained via

$$\tilde{\mathbf{K}}_i = \mathbf{T}\mathbf{K}_i. \qquad (7)$$

Expressing the strain strength in terms of its critical value as $\epsilon = x\epsilon_c$ where we introduce a strain parameter $0 < x < 1$ (cf. Fig. 1),

$$\tilde{\mathbf{K}}_1 = \tilde{k}_0 \begin{pmatrix} \frac{2x}{\sqrt{\nu}} \\ 2 \end{pmatrix},$$

$$\tilde{\mathbf{K}}_{2,3} = \tilde{k}_0 \begin{pmatrix} \pm\sqrt{3} - \frac{x}{\sqrt{\nu}} \\ -1 \pm \sqrt{3\nu}x \end{pmatrix}, \qquad (8)$$

where $\tilde{k}_0 = 2k_0 \sin[\theta/2]$. At the critical strain $x = 1$ all these vectors are multiples of

$$\mathbf{s} = \begin{pmatrix} \frac{1}{\sqrt{\nu}} \\ 1 \end{pmatrix}, \qquad (9)$$

which turns out to depend only on the material specific Poisson ratio and explains the selected direction in the momentum space clearly visible in Figs. 1 and 2.

The real space unit cell is oriented along a direction perpendicular to the vector in Eq. (9),

$$\mathbf{b} = \begin{pmatrix} -\sqrt{\nu} \\ 1 \end{pmatrix}. \qquad (10)$$

Equations (4), (5), (9), and (10) represent central results of our work, and they are valid for any twisted honeycomb lattice system. These quantities depend on the geometry of the twisted moiré lattice only. It suffices to measure only two of the parameters (i.e., twist angle, strain, or Poisson ratio); the third follows from these equations.

We chose the reciprocal lattice vectors of the moiré superlattice to be $\tilde{\mathbf{g}}_1 = \tilde{\mathbf{K}}_3 - \tilde{\mathbf{K}}_1$, $\tilde{\mathbf{g}}_2 = \tilde{\mathbf{K}}_2 - \tilde{\mathbf{K}}_1$ and
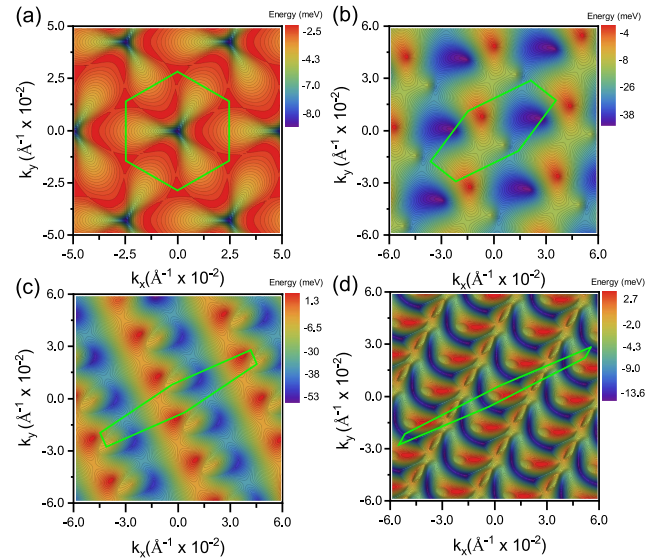

FIG. 2. The evolution of the bottom middle band of TBG with the twist angle $\theta = 1°$ as a function of uniaxial heterostrain with Poisson ratio $\nu = 0.165$ ($\epsilon_c \approx 4.4\%$) and (a) $\epsilon = 0\epsilon_c$, (b) $\epsilon = 0.3\epsilon_c$, (c) $\epsilon = 0.60\epsilon_c$, and (d) $\epsilon = 0.80\epsilon_c$, with ϵ_c denoting the critical strain value defined in Eq. (5). Green hexagons highlight the boundaries of the mBZ.

finally obtained the real space lattice vectors of the distorted lattice in the form

$$\mathbf{L}_1 = \frac{\sqrt{3}a}{4\sin[\theta/2]} \frac{1}{1-x^2} \begin{pmatrix} -\sqrt{3} + x\sqrt{\nu} \\ -1 + x\sqrt{\frac{3}{\nu}} \end{pmatrix}, \quad (11)$$

$$\mathbf{L}_2 = \frac{\sqrt{3}a}{4\sin[\theta/2]} \frac{1}{1-x^2} \begin{pmatrix} \sqrt{3} + x\sqrt{\nu} \\ -1 - x\sqrt{\frac{3}{\nu}} \end{pmatrix}. \quad (12)$$

Note that the length of the vectors $\mathbf{L}_1, \mathbf{L}_2$ diverges at the critical strain, $x \to 1$ as $1/|1-x|$. Below we assume the twist angle θ to be small and keep it to the leading order only. The area of the real space unit cell is

$$A_0 = |\mathbf{L}_1 \times \mathbf{L}_2| = \frac{3\sqrt{3}a^2}{2\theta^2|1-x^2|} \sim \frac{1}{|1-x|} \quad (13)$$

close to the critical strain value. We define the length of the unit cell as

$$L = \frac{|\mathbf{L}_1 + \mathbf{L}_2|}{2} = \frac{3a\sqrt{1+\nu x^2}}{2\theta(1-x^2)} \sim \frac{1}{|1-x|} \quad (14)$$

and the width of the unit cell as

$$W = \frac{|\mathbf{L}_1 \times (\mathbf{L}_1 + \mathbf{L}_2)|}{|\mathbf{L}_1 + \mathbf{L}_2|} = \frac{3a}{2\theta\sqrt{1+\nu x^2}}. \quad (15)$$

The width of the unit cell remains finite at the critical strain, $x \to 1$. Notice that for any values of x larger or smaller than 1 the moiré lattice is reconstructed [40] [cf. Fig. 1(d) and Fig. S3(c) in Ref. [55]].

Near the critical strain, $x \to 1$, the modulations of the moiré lattice in the direction normal to the unit cell, Eq. (9), are determined by the reciprocal lattice vectors, in Eq. (8). The lengths of these vectors are proportional to $1 - \sqrt{3}\nu$ and $1 + \sqrt{3}\nu$. The ratio between these values is, generally, incommensurate. Hence, the properties of the material, near the critical strain, are determined by a unit cell which diverges in one direction, and by combinations of non-commensurate periodicities in the other direction.

Other strain combinations.—The analysis so far has been restricted to uniaxial heterostrains, induced by forces of opposite sign at both layers and at both ends of the sample. Other forces applied at the boundaries can lead to different patterns of strains inside the system. When normal forces are applied to boundaries rotated by 90°, the relation $\epsilon_{yy}/\epsilon_{xx}$ is no longer fixed by the Poisson ratio ν. The pattern is simplified when the periodicities in Eq. (8) are commensurate. This happens when

$$\frac{1 - \sqrt{-\frac{3\epsilon_{yy}}{\epsilon_{xx}}}}{1 + \sqrt{-\frac{3\epsilon_{yy}}{\epsilon_{xx}}}} = \frac{m}{n} \quad (16)$$

where m and n are integers. This equation is satisfied when

$$-\frac{\epsilon_{yy}}{\epsilon_{xx}} = \frac{(m-n)^2}{3(m+n)^2}. \quad (17)$$

The simplest solutions are $m = 0$, $n = 1$, giving $-\epsilon_{yy}/\epsilon_{xx} = 1/3$, and $m = 3$, $n = 1$, giving $-\epsilon_{yy}/\epsilon_{xx} = 1/12$ [cf. Figs. 3(c) and 3(d)]. Then, the properties of the system are determined by a single periodicity, and the pattern at the critical strain reduces to a one-dimensional
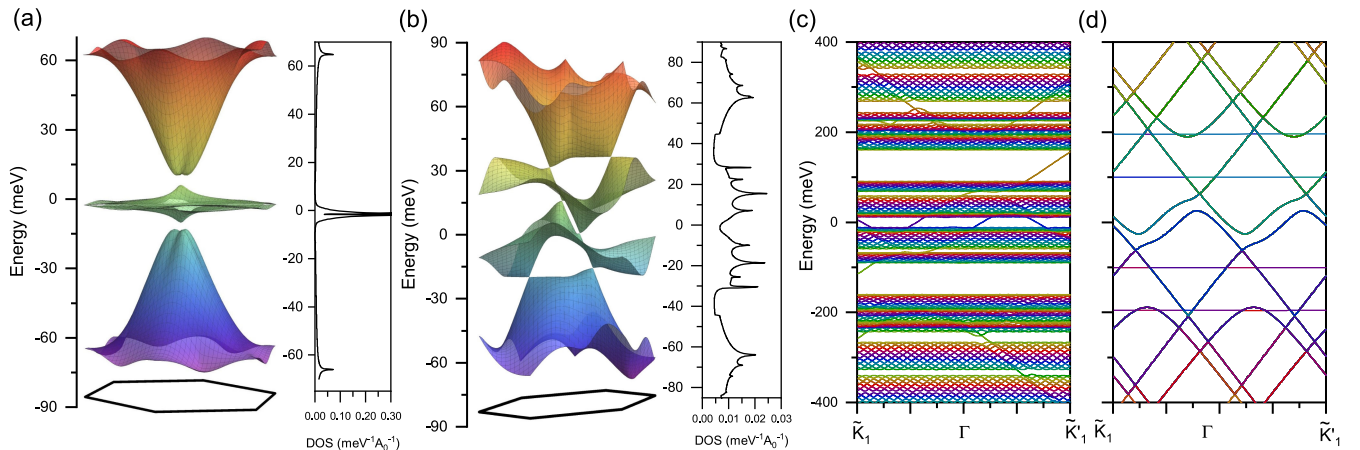

FIG. 3. (a),(b) Evolution of the band structure and DOS of TBG with the twist angle $\theta = 1.0°$ as a function of the uniaxial heterostrain with Poisson ratio $\nu = 0.165$ ($\epsilon_c \approx 4.4\%$) and (a) $\epsilon = 0\epsilon_c$, (b) $\epsilon = 0.20\epsilon_c$. The corresponding mBZ is shown underneath each spectrum. (c),(d) Band structures of the critically strained TBG for $\theta = 1°$ and different values of the ratio between applied strains: (c) $-\epsilon_{yy}/\epsilon_{xx} = 0.165$ and (d) $-\epsilon_{yy}/\epsilon_{xx} = 1/3$. The spectra are evaluated along the collapsed mBZ zone depicted in Fig. 1.

lattice of *AA*, *AB*, and *BA* stripes as shown in Figs. 1(c) and 1(d) (see also Fig. S1 in the Supplemental Material [55]).

Nonhomogeneous strain distributions.—As the size of the moiré unit cell near the critical strain diverges, small local variations of the strain can lead to large changes of the moiré pattern [52]. This is consistent with several recent experimental studies, where the creation of different types of moiré lattice defects has been reported. These are for instance the domain walls between different stacking domains in TBG [40], hexagonal boron nitride [41], or transition metal dichalcogenides [43]. In Fig. 1(d) we show a strain-induced inhomogeneous moiré pattern, where the strain increases in the direction indicated by the black arrows. Here, the moiré pattern interpolates continuously between the minimal and maximal strain. The red arrow points to the region, where the formation of the edge domain wall occurs. This particular inhomogeneous pattern is constructed by a linear combination of the lattice vectors defined in Eqs. (11) and (12). Such inhomogeneous patterns have a strong resemblance to those reported in Refs. [41,43,49,52,68].

Electronic spectrum and the density of states of twisted bilayer graphene with strain.—We now turn our attention to TBG and focus on the twist angle near the first magical angle, $\theta = 1°$. Because of the vector potential defined in Eq. (S6) in the Supplemental Material [55], in a strained TBG the Dirac points no longer reside at the corners of the mBZ (cf. Fig. 2). As strain increases, the Dirac points of the middle bottom band shown in Fig. 2 move on an involved trajectory within the mBZ, which is influenced by several factors, e.g., the geometry of the deformed mBZ and interlayer coupling between graphene layers. More details can be found in the Supplemental Material [55].

Electronic properties of the TBG's continuum model at the critical strain.—As mentioned earlier, at the critical strain the electronic wave functions are determined by the competition between the two, usually incommensurate, periodicities shown in Eq. (16) [see also Eq. (S11) in the Supplemental Material [55]]. The resulting equations resemble the Harper equation [69], extensively discussed in connection to lattice electrons in a constant magnetic field. Systems described by variations of the Harper's equation typically show a discontinuous density of states, and either localized or extended states [56,57,70–74]. We present results for the electronic states for commensurate and incommensurate periodicities, and a twist angle $\theta = 1°$, in Figs. 3(c) and 3(d) (cf. also Fig. S5 in the Supplemental Material [55]). The bands are plotted in a mBZ defined by the sum of the two periodicities. For incommensurate combinations, the results are consistent with extended, i.e., dispersive, states [75], and a singular spectrum, with gaps of different sizes.

Conclusions.—We have presented a general geometry based approach to the strained bilayer graphene. It can be easily adopted to the larger class of strained and twisted bilayer systems. We have found simple expressions for the critical strain, at which the formation of one-dimensional striplike moiré patterns occurs. We find that the formation of such patterns is a consequence of the interplay between twist and strain which gives rise to a collapsing of the reciprocal space unit cell. The criterion for this transition appears to be a very simple relation between the applied uniaxial strain, the twist angle, and the material dependent Poisson ratio. Our results offer simple explanations for the complex patterns of one-dimensional channels observed in low angle twisted bilayer graphene systems and twisted bilayer dicalcogenides. The electronic bands in twisted bilayer graphene in the one-dimensional regime are described by the interplay between two different, typically incommensurate, periodicities, suggesting similarities with the Harper equation and with one-dimensional quasicrystals.

[*]andreas.sinner@uni.opole.pl
[†]panta2mi@gmail.com

[1] J. M. B. Lopes dos Santos, N. M. R. Peres, and A. H. Castro Neto, Phys. Rev. Lett. **99**, 256802 (2007).

[2] S. Shallcross, S. Sharma, and O. A. Pankratov, Phys. Rev. Lett. **101**, 056803 (2008).

[3] S. Shallcross, S. Sharma, E. Kandelaki, and O. A. Pankratov, Phys. Rev. B **81**, 165105 (2010).

[4] R. Bistritzer and A. H. MacDonald, Proc. Natl. Acad. Sci. U.S.A. **108**, 12233 (2011).

[5] G. T. de Laissardière, D. Mayou, and L. Magaud, Nano Lett. **10**, 804 (2010).

[6] E. J. Mele, Phys. Rev. B **81**, 161405(R) (2010).

[7] L. Xian, M. Claassen, D. Kiese, M. M. Scherer, S. Trebst, D. M. Kennes, and A. Rubio, Nat. Commun. **12**, 5644 (2021).

[8] M. Angeli and A. H. MacDonald, Proc. Natl. Acad. Sci. U.S.A. **118**, e2021826118 (2021).

[9] M. H. Naik and M. Jain, Phys. Rev. Lett. **121**, 266401 (2018).

[10] F. Wu, T. Lovorn, E. Tutuc, and A. H. MacDonald, Phys. Rev. Lett. **121**, 026402 (2018).

[11] Y. Tang, L. Li, T. Li, Y. Xu, S. Liu, K. Barmak, K. Watanabe, T. Taniguchi, A. H. MacDonald, J. Shan, and K. F. Mak, Nature (London) **579**, 353 (2020).

[12] E. C. Regan, D. Wang, C. Jin, M. I. B. Utama, B. Gao, X. Wei, S. Zhao, W. Zhao, Z. Zhang, K. Yumigeta, M. Blei, J. D. Carlström, K. Watanabe, T. Taniguchi, S. Tongay, M. Crommie, A. Zettl, and F. Wang, Nature (London) **579**, 359 (2020).

[13] L. Wang, E.-M. Shih, A. Ghiotto, L. Xian, D. A. Rhodes, C. Tan, M. Claassen, D. M. Kennes, Y. Bai, B. Kim, K. Watanabe, T. Taniguchi, X. Zhu, J. Hone, A. Rubio, A. N. Pasupathy, and C. R. Dean, Nat. Mater. **19**, 861 (2020).

[14] G. X. Ni, H. Wang, B.-Y. Jiang, L. X. Chen, Y. Du, Z. Y. Sun, M. D. Goldflam, A. J. Frenzel, X. M. Xie, M. M. Fogler, and D. N. Basov, Nat. Commun. **10**, 4360 (2019).

[15] L. Xian, D. M. Kennes, N. Tancogne-Dejean, M. Altarelli, and A. Rubio, Nano Lett. **19**, 4934 (2019).

[16] G. Oster and Y. Nishijima, Sci. Am. **208**, 54 (1963), https://www.jstor.org/stable/24936147.

[17] G. Oster, M. Wasserman, and C. Zwerling, J. Opt. Soc. Am. **54**, 169 (1964).

[18] E. Y. Andrei, D. K. Efetov, P. Jarillo-Herrero, A. H. MacDonald, K. F. Mak, T. Senthil, E. Tutuc, A. Yazdani, and A. F. Young, Nat. Rev. Mater. **6**, 201 (2021).

[19] Y. Cao, V. Fatemi, S. Fang, K. Watanabe, T. Taniguchi, E. Kaxiras, and P. Jarillo-Herrero, Nature (London) **556**, 43 (2018).

[20] Y. Cao, V. Fatemi, A. Demir, S. Fang, S. L. Tomarken, J. Y. Luo, J. D. Sanchez-Yamagishi, K. Watanabe, T. Taniguchi, E. Kaxiras, R. C. Ashoori, and P. Jarillo-Herrero, Nature (London) **556**, 80 (2018).

[21] F. Mesple, A. Missaoui, T. Cea, L. Huder, F. Guinea, G. Trambly de Laissardière, C. Chapelier, and V. T. Renard, Phys. Rev. Lett. **127**, 126405 (2021).

[22] N. P. Kazmierczak, M. V. Winkle, C. Ophus, K. C. Bustillo, S. Carr, H. G. Brown, J. Ciston, T. Taniguchi, K. Watanabe, and D. K. Bediako, Nat. Mater. **20**, 956 (2021).

[23] T. A. de Jong, T. Benschop, X. Chen, E. E. Krasovskii, M. J. A. de Dood, R. M. Tromp, M. P. Allan, and S. J. van der Molen, Nat. Commun. **13**, 70 (2022).

[24] L. Zhang, Y. Wang, R. Hu, P. Wan, O. Zheliuk, M. Liang, X. Peng, Y.-J. Zeng, and J. Ye, Nano Lett. **22**, 3204 (2022).

[25] M. Vozmediano, M. Katsnelson, and F. Guinea, Phys. Rep. **496**, 109 (2010).

[26] Y. Liu, J. N. B. Rodrigues, Y. Z. Luo, L. Li, A. Carvalho, M. Yang, E. Laksono, J. Lu, Y. Bao, H. Xu, S. J. R. Tan, Z. Qiu, C. H. Sow, Y. P. Feng, A. H. C. Neto, S. Adam, J. Lu, and K. P. Loh, Nat. Nanotechnol. **13**, 828 (2018).

[27] D. A. Cosma, J. R. Wallbank, V. Cheianov, and V. I. Fal'ko, Faraday Discuss. **173**, 137 (2014).

[28] B. Amorim, A. Cortijo, F. de Juan, A. Grushin, F. Guinea, A. Gutiérrez-Rubio, H. Ochoa, V. Parente, R. Roldán, P. San-Jose, J. Schiefele, M. Sturla, and M. Vozmediano, Phys. Rep. **617**, 1 (2016).

[29] G. G. Naumis, S. Barraza-Lopez, M. Oliva-Leyva, and H. Terrones, Rep. Prog. Phys. **80**, 096501 (2017).

[30] L. Huder, A. Artaud, T. Le Quang, G. T. de Laissardière, A. G. M. Jansen, G. Lapertot, C. Chapelier, and V. T. Renard, Phys. Rev. Lett. **120**, 156405 (2018).

[31] Z. Bi, N. F. Q. Yuan, and L. Fu, Phys. Rev. B **100**, 035448 (2019).

[32] Y. Hasegawa, R. Konno, H. Nakano, and M. Kohmoto, Phys. Rev. B **74**, 033413 (2006).

[33] B. Wunsch, F. Guinea, and F. Sols, New J. Phys. **10**, 103027 (2008).

[34] V. M. Pereira, A. H. Castro Neto, and N. M. R. Peres, Phys. Rev. B **80**, 045401 (2009).

[35] G. Montambaux, F. Piéchon, J.-N. Fuchs, and M. O. Goerbig, Phys. Rev. B **80**, 153412 (2009).

[36] M. Oliva-Leyva and G. G. Naumis, Phys. Rev. B **88**, 085430 (2013).

[37] M. Oliva-Leyva and G. G. Naumis, Phys. Lett. A **379**, 2645 (2015).

[38] F. Guinea and N. R. Walet, Phys. Rev. B **99**, 205134 (2019).

[39] P. A. Pantaleón, V. o. T. Phong, G. G. Naumis, and F. Guinea, Phys. Rev. B **106**, L161101 (2022).

[40] J. S. Alden, A. W. Tsen, P. Y. Huang, R. Hovden, L. Brown, J. Park, D. A. Muller, and P. L. McEuen, Proc. Natl. Acad. Sci. U.S.A. **110**, 11256 (2013).

[41] C. R. Woods, P. Ares, H. Nevison-Andrews, M. J. Holwill, R. Fabregas, F. Guinea, A. K. Geim, K. S. Novoselov, N. R. Walet, and L. Fumagalli, Nat. Commun. **12**, 347 (2021).

[42] C. D. Mendoza, I. J. Califrer, and F. L. F. Jr, Appl. Surf. Sci. **544**, 148884 (2021).

[43] S. Shabani, D. Halbertal, W. Wu, M. Chen, S. Liu, J. Hone, W. Yao, D. N. Basov, X. Zhu, and A. N. Pasupathy, Nat. Phys. **17**, 720 (2021).

[44] N. P. Kazmierczak, M. V. Winkle, C. Ophus, K. C. Bustillo, S. Carr, H. G. Brown, J. Ciston, T. Taniguchi, K. Watanabe, and D. K. Bediako, Nat. Mater. **20**, 956 (2021).

[45] T. A. de Jong, T. Benschop, X. Chen, E. E. Krasovskii, M. J. A. de Dood, R. M. Tromp, M. P. Allan, and S. J. van der Molen, Nat. Commun. **13**, 70 (2022).

[46] T. A. de Jong, L. Visser, J. Jobst, R. M. Tromp, and S. J. van der Molen, Phys. Rev. Mater. **7**, 034001 (2023).

[47] M. Kapfer et al., Science **381**, 677 (2023).

[48] N. Tilak, G. Li, T. Taniguchi, K. Watanabe, and E. Y. Andrei, Nano Lett. **23**, 73 (2022).

[49] V. Hsieh, D. Halbertal, N. R. Finney, Z. Zhu, E. Gerber, M. Pizzochero, E. Kucukbenli, G. R. Schleder, M. Angeli, K. Watanabe, T. Taniguchi, E.-A. Kim, E. Kaxiras, J. Hone, C. R. Dean, and D. N. Basov, Nano Lett. **23**, 3137 (2023).

[50] I. M. Craig, M. Van Winkle, C. Groschner, K. Zhang, N. Dowlatshahi, Z. Zhu, T. Taniguchi, K. Watanabe, S. M. Griffin, and D. K. Bediako, arXiv:2303.09662.

[51] T. Peña, A. Dey, S. A. Chowdhury, A. Azizimanesh, W. Hou, A. Sewaket, C. Watson, H. Askari, and S. M. Wu, Appl. Phys. Lett. **122**, 143101 (2023).

[52] R. Engelke, H. Yoo, S. Carr, K. Xu, P. Cazeaux, R. Allen, A. M. Valdivia, M. Luskin, E. Kaxiras, M. Kim, J. H. Han, and P. Kim, Phys. Rev. B **107**, 125413 (2023).

[53] E. J. Mele, Phys. Rev. B **81**, 161405(R) (2010).

[54] J. M. B. Lopes dos Santos, N. M. R. Peres, and A. H. Castro Neto, Phys. Rev. B **86**, 155449 (2012).

[55] See Supplemental Material at http://link.aps.org/supplemental/10.1103/PhysRevLett.131.166402, which cites Refs. [1,4,24,27,31,38,39,54,56–65] for additional results, commensurate conditions and electronic structures.

[56] A. Timmel and E. J. Mele, Phys. Rev. Lett. **125**, 166803 (2020).

[57] A. Timmel and E. J. Mele, Phys. Rev. B **104**, 075419 (2021).

[58] P. San-Jose, J. González, and F. Guinea, Phys. Rev. Lett. **108**, 216802 (2012).

[59] J. González, Phys. Rev. B **94**, 165401 (2016).

[60] V. o. T. Phong and E. J. Mele, Phys. Rev. Lett. **125**, 176404 (2020).

[61] L. Molino, L. Aggarwal, V. Enaldiev, R. Plumadore, V. Falko, and A. Luican-Mayer, arXiv:2210.03074.

[62] P. A. Pantaleón, T. Low, and F. Guinea, Phys. Rev. B **103**, 205403 (2021).

[63] D. K. Efimkin and A. H. MacDonald, Phys. Rev. B **98**, 035404 (2018).

[64] N. R. Walet and F. Guinea, 2D Mater. **7**, 015023 (2019).

[65] C. De Beule, F. Dominguez, and P. Recher, Phys. Rev. Lett. **125**, 096402 (2020).

[66] Y. Bai, L. Zhou, J. Wang, W. Wu, L. J. McGilly, D. Halbertal, C. F. B. Lo, F. Liu, J. Ardelean, P. Rivera, N. R. Finney, X.-C. Yang, D. N. Basov, W. Yao, X. Xu, J. Hone, A. N. Pasupathy, and X.-Y. Zhu, Nat. Mater. **19**, 1068 (2020).

[67] R. Zhang, V. Koutsos, and R. Cheung, Appl. Phys. Lett. **108**, 042104 (2016).

[68] P. Cazeaux, D. Clark, R. Engelke, P. Kim, and M. Luskin, J. Elast., (2023).

[69] P. G. Harper, Proc. Phys. Soc. London Sect. A **68**, 874 (1955).

[70] J. B. Sokoloff, Phys. Rev. B **23**, 2039 (1981).

[71] J. B. Sokoloff, Phys. Rev. B **23**, 6422 (1981).

[72] D. J. Thouless and Q. Niu, J. Phys. A **16**, 1911 (1983).

[73] F. Nori and J. P. Rodriguez, Phys. Rev. B **34**, 2207 (1986).

[74] P. A. Kalugin, A. Y. Kitaev, and L. S. Levitov, Zh. Eksp. Teor. Fiz. **91**, 693 (1986).

[75] It is worth noting that the velocity extracted from the bands in Figs. 3(c) and 3(d) is similar to the Fermi velocity in independent graphene layers. We will not consider here the role of interactions and the possibility that they may lead to Luttinger liquid behavior.